

Research Article

Thermo-Hydro-Mechanical Combined Effect Analysis Model for Early-Age Concrete Bridges and Its Application

Shiwei Li ^{1,2}, Yongqing Yang,¹ Qianhui Pu,¹ Wangqing Wen,² and Aiguo Yan²

¹College of Civil Engineering, Southwest Jiaotong University, Chengdu 610031, China

²China Railway Siyuan Survey and Design Group Company Limited, Wuhan 430063, China

Correspondence should be addressed to Shiwei Li; lishiwei1987@my.swjtu.edu.cn

Received 25 April 2020; Revised 20 August 2020; Accepted 27 August 2020; Published 7 September 2020

Academic Editor: Andreas Lampropoulos

Copyright © 2020 Shiwei Li et al. This is an open access article distributed under the Creative Commons Attribution License, which permits unrestricted use, distribution, and reproduction in any medium, provided the original work is properly cited.

The early cracking of concrete beam bridges remains a concern in civil engineering. An analytical model considering the combined effect of thermo-hydro-mechanical processes forms the basis for assessing the cracking risk of girders during construction. Based on the equivalent hydration theory, the temperature and moisture conduction processes and the evolution of the mechanical properties of concrete were modeled as a function of the equivalent age. A coupling model for the temperature and moisture fields was established, and a theoretical framework for analyzing the thermo-hydro-mechanical combined effect was presented. Based on this, a numerical analysis method was proposed and implemented into ABAQUS; the results were validated with some typical tests. Finally, a long-span prestressed concrete (PC) box girder bridge with balanced cantilever construction was taken as an example, and the causes of web cracking and its impact degree were analyzed. The results show that the rate of moisture conduction is significantly lower than the rate of temperature conduction; even for thin-walled components, there exists a significant humidity gradient on the surface layer. The humidity-induced shrinkage and restraint of the precast members are the main causes of web cracking.

1. Introduction

During the setting and hardening period, concrete is subjected to the combined effect of hydration heat, ambient temperature and humidity, shrinkage and creep, and self-weight, that is, the combined effect of thermo-hydro-mechanical processes [1, 2]. This leads to elastic and inelastic deformations. If these deformations are constrained by internal or external conditions, an additional stress will be developed in the concrete. Moreover, the mechanical properties of concrete materials vary with time. When the combined effect exceeds the resistance of the materials, irreversible damage occurs [3, 4].

When the damage due to the combined effect of thermo-hydro-mechanical processes accumulates to a certain extent, early-age cracks are induced in the concrete. The early-age cracking of concrete bridges is a universal phenomenon. Subramaniam [5] investigated the cracking of concrete bridge decks in New York and found that a large number of

cracks occurred within 48 h of concrete pouring. Li [6] investigated eight concrete girder bridges under construction in Northeast China and found that the main girder concrete cracked to different degrees during the hardening process. Any irreversible damage to concrete bridges in the process of completion can significantly affect the construction quality and structural durability.

The focus in practical applications is on the prevention of nonstructural cracks. However, the preventive measures are ineffective because of the poor understanding of the cracking mechanism. The cracking phenomenon remains to be quite frequent during construction [7]. The role of single factors in the formation of cracks is often emphasized. Li [6] focused on the mechanism of cracking induced by shrinkage. Huang et al. [8] attributed the cracking of concrete girders to excessive early hydration heat. For concrete bridges, the concrete mix ratio is varied, the ambient environment is complex and dynamic, and the temperature and humidity conduction processes in concrete have coupling

characteristics [9, 10]. Therefore, it is necessary to establish a suitable method to analyze the combined effect of the thermo-hydro-mechanical processes.

To analyze this combined effect during concrete hardening, much research has been devoted to this subject in recent decades. Ulm and Coussy [11, 12] proposed a thermo-chemomechanical model for the prediction of deformation and cracking accounting for strength growth through chemoplastic coupling within the theory of elastoplasticity, but the effects of creep and relative humidity were not considered. Cervera et al. [13, 14] formulated a coupled thermo-chemo-mechanical model for the behavior of concrete at early ages, but the effect of the relative humidity is not considered. Lackner and Mang [15] proposed a chemo-mechanical model for early-age cracking of concrete in which the effect of relative humidity is also neglected. Gawin et al. [16, 17] developed a hydro-thermal-chemo-mechanical model of concrete at early ages which comprehensively accounts for the aging and hydrothermal coupling but lacks a comprehensive constitutive law for early-age concrete. Di Luzio and Cusatis [18] proposed the solidification-microprestress-microplane (SMM) model describing the mechanical behavior of concrete at early age under variable hydrothermal conditions. Cui et al. [19] formulated a sequential coupling analysis method for concrete members; however, those models cannot be applied to the sequential casting of multisegment concrete bridges, and they do not consider the restraint of steel bars on shrinkage deformation and its contribution to crack resistance.

In this study, to accurately analyze the thermo-hydro-mechanical combined effect in the construction process of concrete bridges, the temperature and moisture conduction processes and the evolution of the mechanical properties of concrete were modeled as a function of the equivalent age based on the equivalent hydration theory. A coupling model for the temperature and moisture fields was established, and a theoretical framework for the combined effect analysis was presented. The corresponding numerical analysis method was proposed and implemented into ABAQUS; the results were validated by conducting some typical tests. Finally, a long-span prestressed concrete (PC) box girder bridge with balanced cantilever construction was taken as an example, and the causes of web cracking and its impact degree were analyzed.

2. Coupling Analysis Theory of Temperature and Moisture Fields

2.1. Theory of Temperature Conduction. Due to the combined effect of hydration heat and ambient environment (atmospheric temperature and solar radiation), concrete remains in a dynamic thermal equilibrium with the external environment. During concrete hardening, the temperature field of concrete is mainly driven by hydration heat. When the hydration reaction is largely completed, the temperature field is mainly driven by the ambient temperature. Because of the influence of temperature conduction rate, the

response of the internal temperature of concrete lags behind the change in the ambient temperature.

2.1.1. Hydration Heat. The active chemical components in the cement clinker react with the mixing water, releasing a lot of heat. The total heat release (H_{total}) considering the influence of clinker composition can be calculated as [20]

$$H_{\text{total}} = 500C_3S + 260C_2S + 866C_3A + 420C_4AF + 1186\text{free Cao} + 850\text{MgO} + 624\text{SO}_3 + 461\text{slag} + \text{FA}(15.9(100p_{\text{CaO}}) + 74.3), \quad (1)$$

where, C_3S , C_2S , C_3A , and C_4AF are the mass ratios of each chemical component; free CaO is the mass ratio of free calcium oxide in the cement; slag indicates blast furnace slag; FA is the mass ratio of fly ash; and p_{CaO} is the proportion ratio of CaO in FA.

When the active chemical components in cement clinker cannot be accurately obtained, H_{total} can be calculated as [21]

$$H_{\text{total}} = Q_0(W + kF), \quad (2)$$

where W is the amount of cement; F is the amount of admixture; k is the coefficient of reduction and equals 0.25 for fly ash; Q_0 is a constant for heat of hydration of cement and equals 330 kJ/m^3 for silicate cement 425# or 525#.

The hydration heat release ($H(t)$) at different times can be expressed as a function of the equivalent age (t_e), as shown in

$$H(t) = H_{\text{total}}\alpha(t_e), \quad (3)$$

where $\alpha(t_e)$ is a function of the hydration degree and is related to t_e . It can be expressed as

$$\alpha(t_e) = \frac{H(t)}{H_{\text{total}}} = \alpha_u e^{(-\eta t_e)^\beta}, \quad (4)$$

where η is the hydration time parameter and β is the hydration rate parameter, both of which are related to the clinker composition, cement fineness, and admixture; α_u is the ultimate degree of hydration; η , β , and α_u are obtained by

$$\left\{ \begin{array}{l} \beta = C_3S^{0.280} \cdot C_3S^{0.143} \cdot \text{SO}_3^{0.1378} \cdot \text{Blaine}^{-0.994}, \\ \eta = 2.649C_3S^{-0.541} \cdot C_3S^{-0.122} \cdot \text{SO}_3^{-1.191} \cdot \text{Blaine}^{-0.567}, \\ e^{0.318\text{slag}+8.365\text{FA.FA}_{\text{CaO}}}, \\ \alpha_u = \frac{1.031w/c}{(0.194 + w)/c} + 0.361\text{FA} + 4.285 \text{slag}, \\ (0.730\text{HI} - 1) \leq 1, \end{array} \right. \quad (5)$$

where Blaine is the fineness coefficient of cement ($\text{m}^2 \cdot \text{kg}^{-1}$); FA_{CaO} is the mass ratio of CaO to FA; w/c is the water-cement ratio; HI is the hydraulic index and can be expressed as

$$\text{HI} = \frac{\text{CaO} + \text{MgO} + \text{Al}_2\text{O}_3}{\text{SiO}_2} \quad (6)$$

where CaO, MgO, Al₂O₃, and SiO₂ are the mass ratios of each chemical component with respect to the admixtures.

t_e considering the temperature history is given by

$$t_e = \int_0^t e^{-(E_A/R)(1/273+T-(1/(273+T_{\text{ref}})))} dt. \quad (7)$$

where E_A is the activation energy; for $T \geq 20^\circ\text{C}$, $E_A = 33.5 \text{ kJ}\cdot\text{mol}^{-1}$, and $T < 20^\circ\text{C}$, $E_A = 33.5 + 1.47 \times (293 - T)$ ($\text{kJ}\cdot\text{mol}^{-1}$); R is the universal gas constant; and T_{ref} is the reference temperature, which is typically 20°C .

2.1.2. Temperature Conduction. According to the principle of thermal equilibrium, the heat absorbed due to an increase in the structural temperature is equal to the sum of internal hydration heat and external inflow heat [22]. According to Fourier heat conduction theory, the differential equation for concrete temperature conduction can be expressed as [20]

$$\rho c(t_e) \frac{\partial T}{\partial \tau} = k(\alpha(t_e)) \nabla^2 T + \rho c(t_e) \xi(h) \frac{\partial H(t)}{\partial \tau}, \quad (8)$$

$$k(\alpha(t_e)) = k_u \cdot (1.33 - 0.33\alpha(t_e)), \quad (9)$$

$$c(t_e) = \frac{(W_c \alpha(t_e) c_{\text{cef}} + W_c (1 - \alpha(t_e)) c_c + W_a c_a + W_w c_w)}{\rho}, \quad (10)$$

$$\xi(h) = \frac{1}{1 + 4(5 - 5h)}. \quad (11)$$

where k is the current thermal conductivity; k_u is the thermal conductivity of hardened concrete; c is the specific heat of concrete; h is the relative humidity; ξ is the influence coefficient of humidity on temperature conduction; ρ is the density of concrete; W_c , W_a , and W_w are the amounts of cement, aggregate, and water, respectively, by weight; c_c , c_a , and c_w are the specific heats of aggregate, cement, and water, respectively; c_{cef} is the fictitious specific heat of the hydrated part of cement and is equal to $(8.4 T_c + 339) \text{ kJ}\cdot\text{kg}^{-1}$.

The thermal conductivity k and specific heat of concrete c are related to the temperature of concrete, while the temperature of concrete is related to its equivalent age t_e . The equivalent age t_e comprehensively reflects the influence of the hydration process and the environmental temperature of concrete. Both k and c are described as functions of t_e , as shown in equation (8). Thus, the key performance parameters of the concrete temperature field evolve with the hydration process.

2.1.3. Initial and Boundary Conditions. The molding temperature of concrete is generally considered the initial condition of temperature conduction.

Based on the different contact conditions between the concrete surface and surrounding media, the boundary conditions can be divided into four types [21]. The heat

transfer between concrete and air is considered based on the third type; this boundary condition can consider the influence of the type and thickness of the mold on the heat transfer of concrete, as shown in equation (12) [20]:

$$\chi_s = \frac{1}{(1/\chi) + \sum h_i/\lambda_i}, \quad (12)$$

where χ_s is the equivalent surface conduction of the concrete surface; χ is the surface conductance; and h_i and λ_i are the thickness and conductivity of the i th layer, respectively.

The heat transfer between the successive segments is considered based on the fourth type of the boundary conditions.

2.2. Theory of Moisture Conduction. Evaporation to the environment and cement hydration reaction are the two main factors leading to the reduction in the moisture content of concrete [23].

2.2.1. Humidity Reduction due to Cement Hydration. Zhang et al. [23] proposed a two-stage calculation model for humidity reduction due to cement hydration based on a humidity conduction test. The model is expressed in

$$H_s = \begin{cases} 1 (\alpha \leq \alpha_c), \\ (H_{\text{su}} - 1) \left(\frac{\alpha - \alpha_c}{\alpha_u - \alpha_c} \right)^k + 1 (\alpha > \alpha_c), \end{cases} \quad (13)$$

where H_{su} is the relative humidity (RH) considering self-desiccation at ultimate degree hydration; α_c is the critical hydration degree at which the humidity inside the concrete starts to decrease from 100% level; and κ is the drying rate parameter.

2.2.2. Moisture Conduction. According to the second Fick's law, the differential equation for concrete moisture conduction can be expressed as [23]

$$\frac{\partial h}{\partial t} = D(h) \nabla^2 h + \frac{\partial H_s}{\partial t}, \quad (14)$$

where H_s is the humidity reduction due to cement hydration and $D(h)$ is the moisture transfer coefficient. Experimental results have shown that $D(h)$ increases rapidly with an increase in the humidity and that the temperature increases the humidity conduction rate, as shown in equation (15) [24]:

$$D(h) = D_1 \left\{ \omega + \frac{1 - \omega}{1 + [(1 - h)/(1 - h_c)]^n} \right\} f(t_e), \quad (15)$$

where D_1 is the maximum $D(h)$ for $h = 100\%$, as shown in equation (16); $\omega = D_0/D_1$, D_0 is minimum $D(h)$ for $h = 0\%$; h_c is the relative pore humidity at $0.5 D_1$; n is an exponent; $f(t_e)$ is the temperature influence function, as shown in equation (17).

$$D_1 = \frac{D_{1.0}}{f_{\text{cm}} - 8}, \quad (16)$$

where $D_{1,0} = 1 \times 10^{-8} \text{ m}^2/\text{s}$ and f_{cm} is the mean compressive strength of concrete expressed in MPa.

$$f(t_e) = e^{((1/R)((U_{aT}/273+T)-(U_{ar}/273+T_{ref}))}, \quad (17)$$

where U_{aT} and U_{ar} are the apparent activation energies at temperature T and at the reference temperature T_{ref} , respectively.

2.2.3. Initial and Boundary Conditions. The initial condition for moisture conduction in poured concrete is generally 100%.

The humidity transfer rate at the concrete surface is related to ambient humidity, wind speed, and temperature. It can be calculated using equation (18) [25]:

$$f(h_{en} - h_{surf}) = f_{boundary}(h_{en} - h_{surf}), \quad (18)$$

where $f_{boundary}$ is a proportionality factor and h_{surf} and h_{en} are the concrete surface humidity and environmental humidity, respectively.

3. Analysis of Stress Field

In addition to the corresponding self-stresses due to the nonuniform temperature and humidity gradients, an additional tensile stress will occur when the shrinkage deformation due to the temperature and humidity fields is constrained. Moreover, creep will cause stress relaxation. Remarkably, when concrete is subjected to the combined effect of thermo-hydro-mechanical processes, its mechanical properties evolve with time.

3.1. Mechanical Parameters of Early-Age Concrete. The elastic modulus E , tensile strengths f_t , and compressive strength f_c of concrete varying with the equivalent age can be expressed as [26]

$$E(t_e) = E_{28} \cdot \left[e^{s(1 - \sqrt{(672/t_e - t_0)})} \right]^{n_E}, \quad (19)$$

$$f_t(t_e) = f_{t28} \cdot \left[e^{s(1 - \sqrt{(672/t_e - t_0)})} \right]^{n_t}, \quad (20)$$

$$f_c(t_e) = f_{c28} \cdot \left[e^{s(1 - \sqrt{(672/t_e - t_0)})} \right]^{n_c}, \quad (21)$$

where E_{28} , f_{t28} , and f_{c28} are the elastic modulus (GPa), tensile strength (MPa), and compressive strength (MPa) of concrete at 28 d, respectively; t_0 is the time at which the concrete strength begins to develop (in h); and the parameters t_0 , s , n_E , and n_t can be taken as 10 h, 0.211, 0.339, and 0.621, respectively, when there is no reliable test data.

3.2. Relationship between Temperature Field Change and Temperature Deformation. Temperature deformation can be expressed as a product of the temperature deformation coefficient and the temperature difference, as shown in

$$\varepsilon_T = \alpha_T \Delta T, \quad (22)$$

where α_T is the temperature deformation coefficient, which is in the range of $1.0-1.2 \times 10^{-5}/^\circ\text{C}$, and ΔT is the temperature difference (in $^\circ\text{C}$).

3.3. Relationship between Humidity Field Change and Shrinkage Deformation. When the relative humidity in the atmosphere is lower than that in concrete, the moisture in the concrete will diffuse to the environment and cause drying shrinkage. The hydration reaction of cement consumes free water in the capillaries of concrete, thus decreasing the interior relative humidity and causing an autogenous shrinkage of concrete [27]. The relationship between moisture-induced shrinkage and interior RH from the time of concrete setting can be expressed as [27]

$$\varepsilon_W = \varepsilon_C + \alpha_h(100 - h), \quad (23)$$

where ε_W is the shrinkage strain, ε_C is the shrinkage during the humidity developing stage I (RH = 100%), which is principally governed by w/c , and α_h is the shrinkage strain due to unit humidity reduction.

3.4. Tensile Creep of Early-Age Concrete. The double power law (DPL) creep model proposed by Bazant and Panula [28] is selected because it has shown good accuracy in many early-age tensile creep tests [29, 30]. The model is expressed in

$$J(t, \tau) = \frac{1}{E(\tau)} + \frac{q}{E(\tau)} \tau^{-d} (t - \tau)^p, \quad (24)$$

where $J(t, \tau)$ is the creep compliance function at time t , τ is the loading age, $E(\tau)$ is the asymptotic elastic modulus, and q , d , and p are the material parameters, calibrated based on experimental concrete creep tests.

3.5. Strength Criterion with Age Evolution. In this study, the Lubliner criterion [31], which has been widely used for concrete in complex stress states, was chosen, as shown in

$$F(\sigma) = \frac{1}{1 - \alpha} \left(\sqrt{3J_2} + \alpha I_1 + \beta \langle \widehat{\sigma}_{\max} \rangle - \gamma \langle -\widehat{\sigma}_{\max} \rangle \right) - f_c(t_e), \quad (25)$$

where $\langle \rangle$ are Macaulay brackets and $\langle x \rangle$ is taken as $((|x| + x)/2)$; I_1 is the first stress invariant; J_2 represents the second deviatoric stress invariant; $\widehat{\sigma}_{\max}$ is the maximum effective stress eigenvalue; α and β are undetermined parameters determined by the uniaxial tensile strength and compressive strength, respectively, and can be taken as 0.12 and 7.68, respectively; γ is equal to 3 in the low confining pressure stress state.

4. Numerical Analysis Method of Thermo-Hydro-Mechanical Combined Effect

To realize the analysis of the thermo-hydro-mechanical combined effect, the temperature and humidity fields of

concrete are determined first, and the additional deformation is then applied to the concrete structure. However, because of the coupling characteristics of the temperature and moisture conduction, iteration at each time step will increase the computing costs significantly. Therefore, the whole iteration method is used. This method does not significantly increase the calculation cost and shows sufficient calculation accuracy. The processes can be described as follows.

First, the initial temperature field is analyzed under the specified humidity environment. According to the environmental characteristics and mix proportion of concrete, the initial and boundary conditions of the temperature field analysis and the relevant basic parameters (c and k) are determined. The temperature field changes at each time step are calculated through the differential equation of the concrete temperature conduction, and the temperature change data at all the nodes in the time history are stored.

The initial humidity field is then analyzed. In addition to determining the initial conditions, boundary conditions, and related calculation parameters ($D(h)$), the results of the temperature field analysis are imported to calculate the humidity conductivity and solve the humidity conduction differential equation. Similarly, the time history humidity data at all the nodes need to be stored.

Finally, the calculation results of the humidity field are imported to the process of temperature field analysis, and a secondary temperature field analysis is carried out.

The above process is a global iteration, and the desired accuracy is achieved after several iterations.

When the temperature and humidity fields of concrete are determined, the stress field can be analyzed. The temperature and humidity data at each time step are used to calculate the additional deformation in terms of the temperature expansion coefficient and humidity deformation coefficient and the mechanical parameters, which vary with the effective age, are also adjusted.

The finite element software ABAQUS and its secondary development platform were selected for this complex process. The core programming steps are described as follows.

Because the differential equations of the temperature and moisture conduction (equations (7) and (13)) have a consistent form, they can be solved using subroutine UMATHT. The boundary conditions of the temperature and humidity conduction are defined by subroutine FILM, which can simulate the change in the temperature and humidity environment with time. The subroutine UEXPAN is used to extract the temperature and humidity data at each time step and calculate the corresponding increment strain. Moreover, the subroutine USDFLD is used to consider the influence of creep. In addition, the evolution of the mechanical parameters is simulated by defining field variables (FIELD). Figure 1 shows the specific process.

5. Model Verification

5.1. Temperature Field Simulation of a Prefabricated Box Girder by Electric Heating. A prefabricated concrete box girder bridge of the Chongqing-Guizhou Railway was

constructed in winter. To accelerate construction, measures of electric heating and insulation layer were employed. To understand the actual effect of these measures, Yao et al. [32] conducted a temperature test.

The length of the test beam was 26.58 m. After 6 h of casting, the inner form was removed, and four electric heaters with a power of 2000 W were evenly installed along the span direction. At the beam-end of the box girder, the retaining wall with masonry was overlapped by a polyethylene foam layer. After 24 h of casting, the outer form was replaced by the polyethylene foam layer. The electric heaters were removed after working for three days; the insulation layer remained overlapped to avoid fast cooling. Table 1 lists the mix proportion of concrete. Figures 2 and 3 show the heating device box girder section and temperature measurement points.

The subroutine UMATHT was used for the temperature field analysis. The concrete was modeled using DC3D8. Based on the field measurements, the hydration heat function can be calculated using (26), and the unit of t_e is h :

$$H(t) = 115500(1 - e^{-0.05t_e}) \text{ kJ}\cdot\text{m}^{-3}. \quad (26)$$

The concrete molding temperature was 20°C. The ambient temperature, which changed only slightly, was approximately taken as 5°C. Based on the measured data, the electric heating inside the box girder is considered by constant thermal radiation (32°C). The equivalent surface conductance of the outer surface of concrete between concrete and thermal insulation layers is $\chi_s = 2 \text{ W}/(\text{m}^2\cdot\text{C})$ and that of the flange end is $\chi_s = 0.5 \text{ W}/(\text{m}^2\cdot\text{C})$. The equivalent surface conductance between concrete and air is $\chi_s = 15 \text{ W}/(\text{m}^2\cdot\text{C})$. The heat conductivity k_u is calculated using equation (9) and taken as $2.618 \text{ W}/(\text{m}^2\cdot\text{C})$. The specific heat capacity c is calculated using equation (10) and taken as $913.22 \text{ J}/(\text{kg}\cdot\text{C})$. The density of concrete is $2497 \text{ kg}\cdot\text{m}^{-3}$.

The results of the temperature measurement at A3 and A4 (as shown in Figure 3) are compared with the simulation results shown in Figure 4; the results are in good agreement, regardless of the peak temperature or the change trend. This demonstrates that the proposed method can effectively simulate the temperature field of concrete bridges.

5.2. Simulation of Moisture Conduction Process and Shrinkage Deformation. Zhang et al. [33] conducted a moisture conduction test on early-age concrete under two drying conditions: only surface sealing (specimen I) and surface sealing followed by exposure to the environment (specimen II). Table 2 lists the concrete mix proportion. The specimens were cuboid-shaped and 400 mm × 100 mm × 60 mm in size. A layer of 1 mm thick polytetrafluoroethylene (PTFE) sheet was laid on the bottom of the specimen to reduce the friction resistance.

Figure 5 shows the test apparatus. The digital temperature and humidity sensors, which are located at the geometric center of the specimen, were used. The free deformation of the concrete was measured using LVDT.

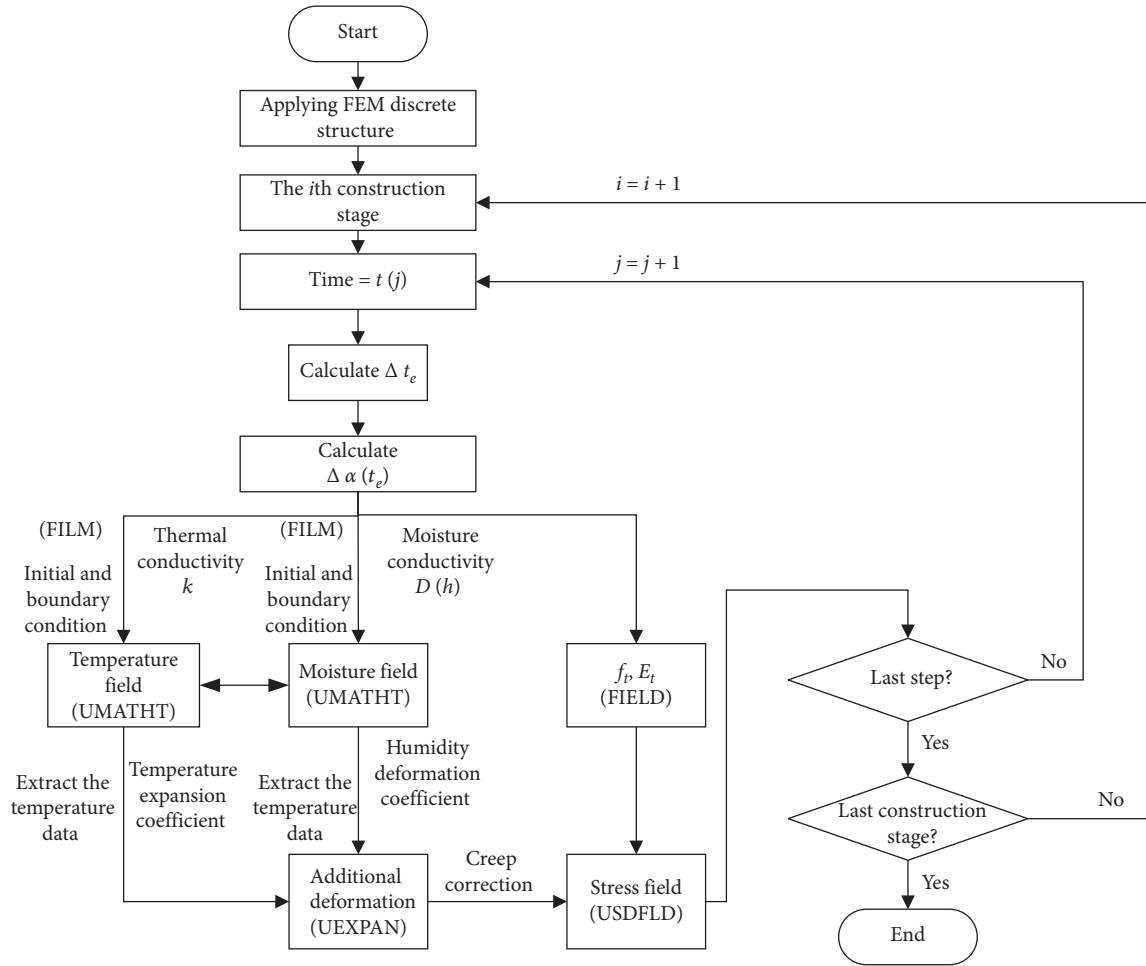


FIGURE 1: Computation program flowchart of thermohydrmechanical combined effect.

TABLE 1: Mix proportion of concrete (kg/m³).

Cement	Fine aggregate	Coarse aggregate	Water	Admixture	Fly ash
323	797	1104	155	10.77	108

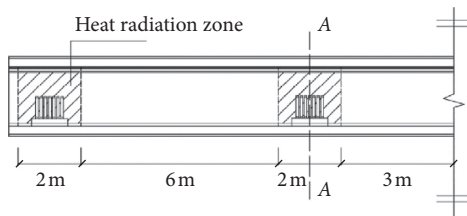


FIGURE 2: Simulation of temperature load [32].

When the density and specific heat of concrete are set to 1, the differential equation of the moisture conduction has the same mathematical form as that of the temperature conduction. Therefore, the moisture field analysis method is consistent with the temperature field analysis method. The concrete was also modeled using DC3D8 with 2300 elements. The ambient temperature and humidity vary only slightly and are taken as 23°C and 16%, respectively. Table 3

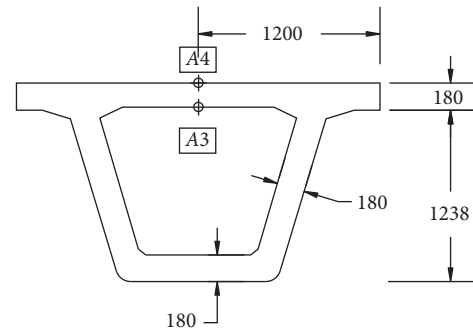


FIGURE 3: Temperature measuring points A3 and A4 of Section A (unit: mm).

lists the other relevant calculation parameters. The deformation due to the change in the humidity is calculated using equation (23); ϵ_c is 210×10^{-6} ; and α_h is $15 \times 10^{-6}/\%$.

Figures 6 and 7 show the humidity change and free deformation of the two specimens. The simulation and actual results are mostly consistent. Figure 8 shows the development of the humidity gradient of specimen I; Figure 9 shows a comparison between the temperature and humidity conduction processes. The results show that the

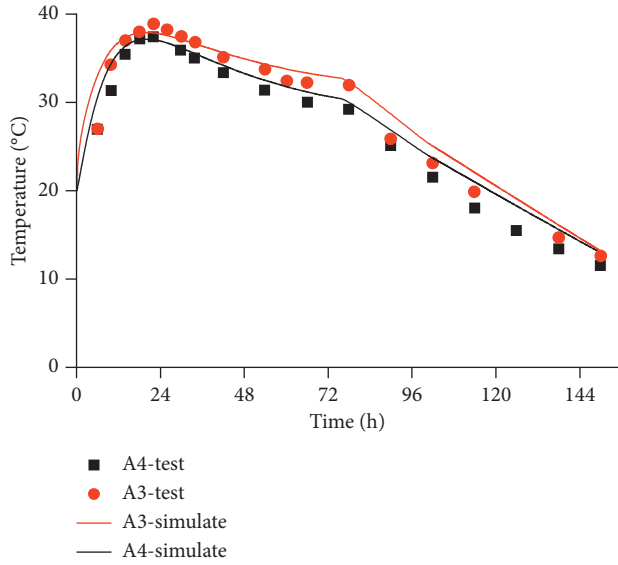


FIGURE 4: Comparison of simulated data and measured data on points A3 and A4.

TABLE 2: Mix proportion of concrete (kg/m³).

Cement	Water	Fine aggregate	Coarse aggregate	Silica fume	Fly ash
345	185	685	1090	—	85



FIGURE 5: Test apparatus of moisture conduction [33].

TABLE 3: Parameters of humidity field.

H_{su}	α_c	κ	ω	h_c (%)	n	$f(h_{en} - h_{surf})/m^2 \cdot h^{-1}$
0.65	0.4909	2.27	0.006	96.9	1.43	0.2×10^{-3}

humidity conduction rate is much lower than the temperature conduction rate; even for the thin-walled components, there remains a significant humidity gradient beneath the surface.

5.3. *Simulation of Tensile Creep in Early-Age Concrete.* To understand the role of tensile creep in early-age concrete, Khan et al. [34] evaluated the creep deformation of concrete dog-bone specimens under a sustained tensile stress. Figure 10 shows the specimen size and loading apparatus.

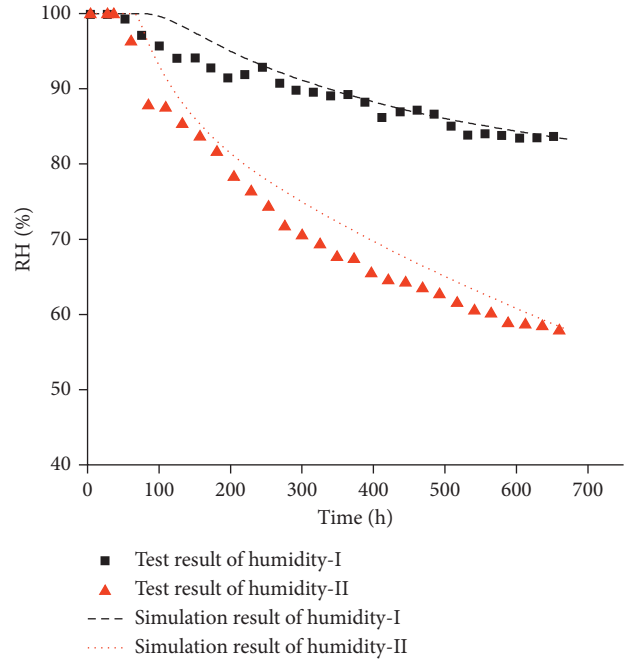


FIGURE 6: Development of interior humidity with age.

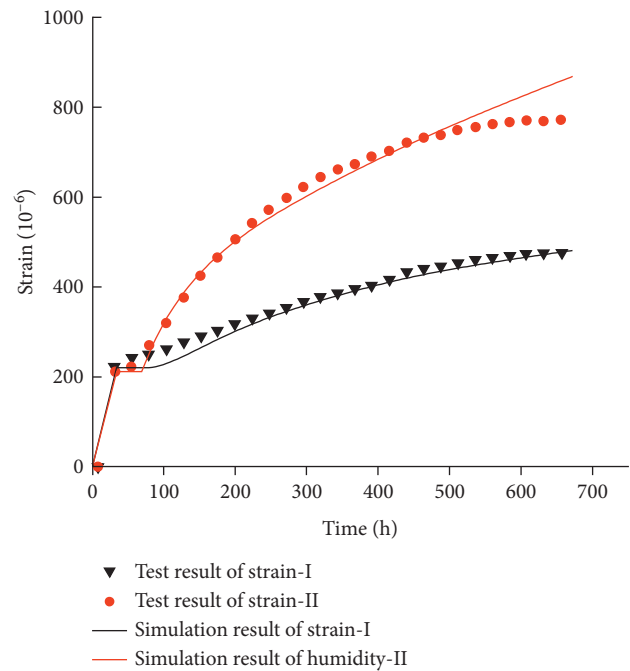


FIGURE 7: Development of free shrinkage strain with age.

Table 4 lists the mix proportion of concrete; Table 5 lists the main mechanical properties.

The loading ages for the dog-bone creep specimens were 1 and 2 d. The loading stress level was 50% of the measured tensile strength at the loading age, that is, 0.7 MPa on day 1 of aging and 1.05 MPa on day 2 of aging.

Two user subroutines (USDFLD and UEXPAN) were required to implement the creep analysis through the ABAQUS secondary development platform. The DPL creep

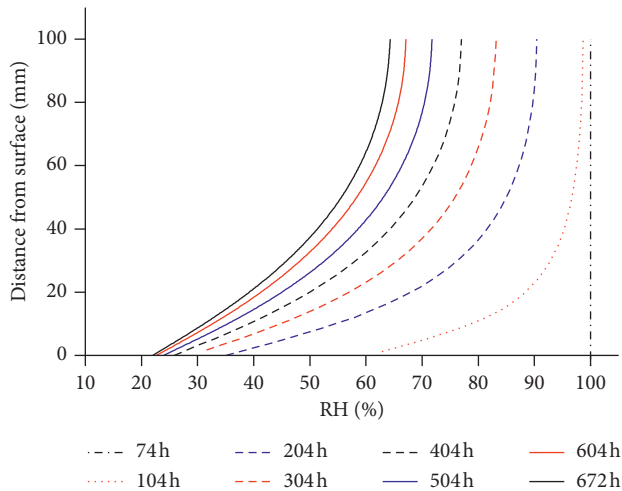


FIGURE 8: Humidity gradient of drying specimens.

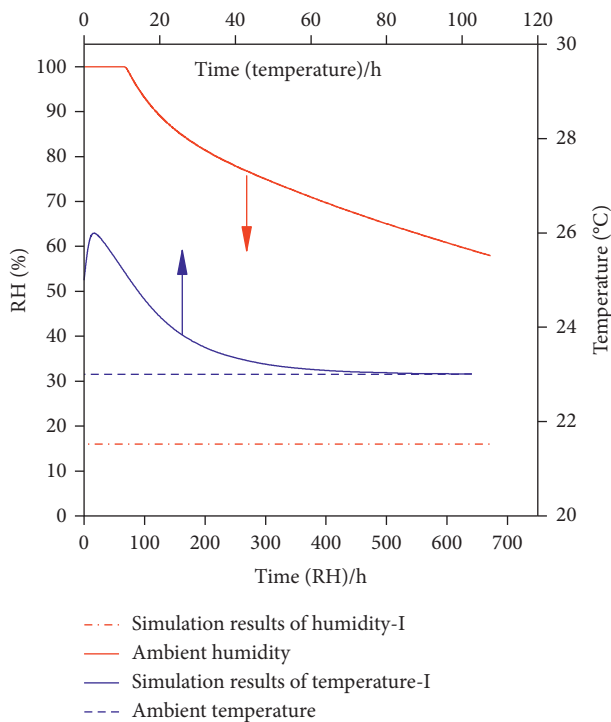


FIGURE 9: Development of interior humidity and temperature with age.

function was chosen for this analysis, as shown in equation (24); q , d , and p are 0.59, 0.26, and 0.41, respectively. Figure 11 shows the simulation and test results of the creep coefficient. The simulated values were closer to the test results.

6. Early-Age Cracking Analysis of a PC Box Girder Bridge with Cantilever Casting

6.1. Engineering Background. A PC box girder bridge with a span of 110+190+100 m was segmentally constructed in 2009. The web thickness varies from 1 m at the 0# block to

0.7 m at the midspan. Visible cracks occurred in 2# block during construction. Wang and Fang evaluated the change in the web temperature of 2# block during hardening in situ [35].

Table 6 lists the mix proportion of the main girder of C60. Figure 12 shows the evolution of the tensile strength and elastic modulus. The diameters of the vertical and transverse steel bars are $\Phi 20$ and $\Phi 12$, respectively. Figure 13 shows the temperature measuring points in the 2# block web.

6.2. Calculation Model. The shrinkage deformation of 2# block is constrained by 1# block. Therefore, to accurately analyze the response of 2# block under the combined action of multifields, the influence of 1# block should be considered. A 1/2 model of 1# block and 2# block with solid elements was constructed considering the symmetry of the structure. The constraint effects on the free deformation and contribution to concrete tension of the steel bar are considered, as shown in Figure 13. Similarly, the subroutines UMATHT and FILM are used to analyze the temperature and humidity conduction processes, and the temperature load and creep correction are realized using the subroutines UEXPAN and USDFLD.

For the temperature and humidity field analysis, the DC3D8 element is used to model the concrete. For the stress field analysis, the C3D8 concrete element and T3D4 rebar element are used to model the concrete girder and steel bar, respectively. The foregoing analysis results show that a significant humidity gradient is formed beneath the surface. Therefore, the thickness of the concrete element near the surface should not be too large, and the mesh should be consistent due to the continuity of the thermo-hydro-mechanical analysis. There are 193596 concrete elements and 19800 rebar elements, as shown in Figure 14. The active and inactive element methods are used to simulate the construction process. The changes in the ambient temperature and humidity are simulated using the subroutine FILM.

The hydration heat function is calculated using (27). The specific heat capacity of the concrete with the change in the effective age is calculated using (10). For the temperature boundary conditions, the ambient temperature is fitted with the sum of several trigonometric functions to the measured value, as shown in (28). When n is taken as 7, the prediction accuracy is good, as shown in Figure 15. k_u and χ_s are taken as 2.6 and 15 W/(m²·°C), respectively. The density of concrete is 2459.7 kg·m⁻³.

$$H(t) = 155512(1 - e^{-0.05t_e}) \text{kJ} \cdot \text{m}^{-3}, \quad (27)$$

$$T(t) = \sum_{i=1}^n a_i \sin(b_i t + c_i). \quad (28)$$

The humidity reduction due to cement hydration reaction is calculated using equation (12). The humidity conductivity coefficient is calculated using the CEB-FIP (2010) formula considering temperature correction, as

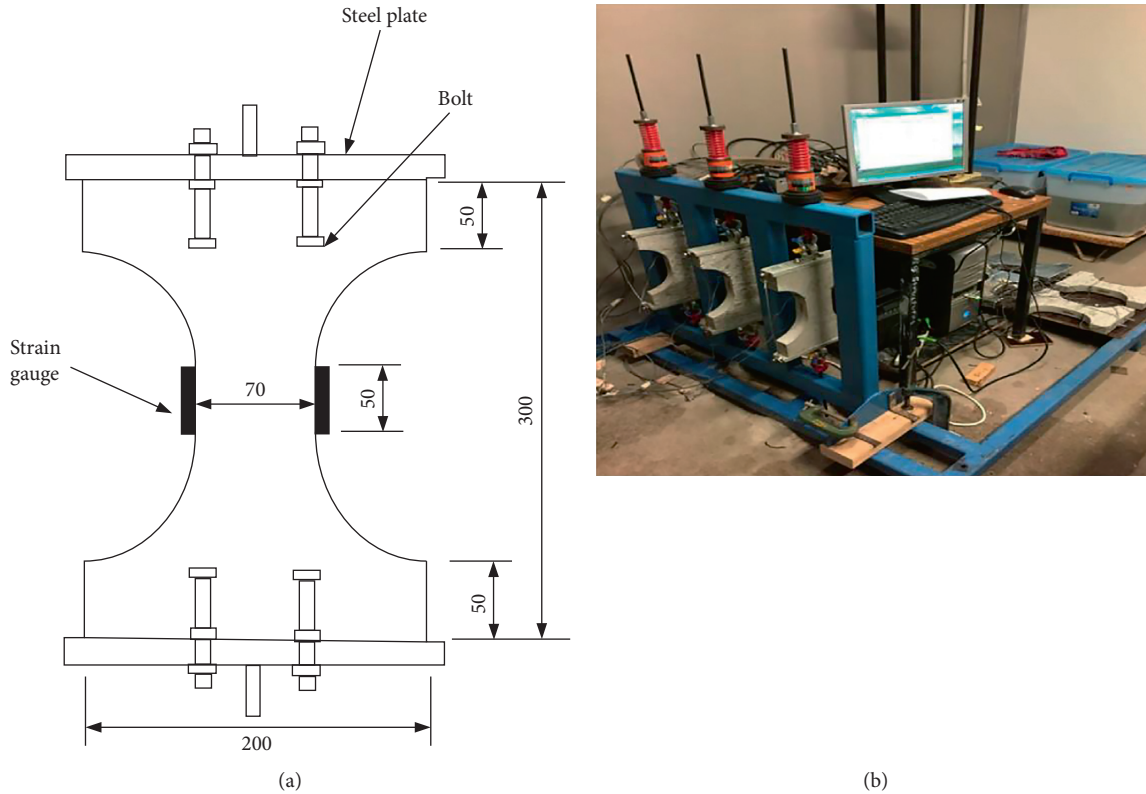


FIGURE 10: Dog-bone specimen and loading apparatus [34].

TABLE 4: Mix proportion of concrete (kg/m³).

Cement	Water	Fine aggregate	Coarse aggregate
380	210	545	1265

TABLE 5: Mechanical characteristics of concrete.

Age (d)	Compressive strength (MPa)	Tensile strength (MPa)	Elastic modulus (GPa)
0.75	13.18	1.2	18.35
1	15.28	1.4	20.35
2	21.55	2.1	22.05
3	24.64	2.54	22.7
7	32	2.94	27.78
28	36	3.47	28.58

shown in equation (15). For the humidity boundary conditions, the main girder concrete should be kept wet during hardening. Therefore, the external humidity environment of the concrete is affected by the level of artificial intervention. To explore the influence of different curing effects on the humidity field, three calculation conditions (60, 80, and 100%) are defined based on the varying environmental humidity. According to the research results obtained by

Oliveira et al. [25], the surface factor f_{boundary} is approximately linear with D_1 , as shown in equation (29):

$$f_{\text{boundary}} = (0.093D_1 - 0.21) \times 10^{-4} \text{m}^2 \cdot \text{s}^{-1}. \quad (29)$$

For the stress field analysis, the evolutions of the tensile strength and elastic modulus can be calculated using equations (19) and (20). The stress relaxation due to the creep is calculated using (24). q , d , and p are taken as 0.6, 0.2,

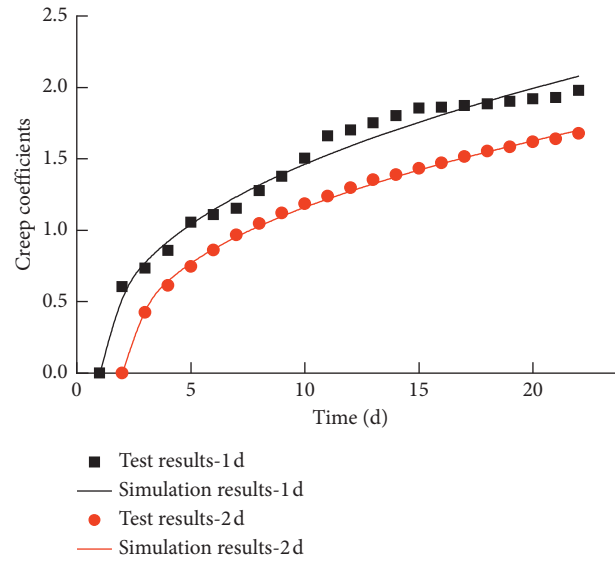


FIGURE 11: Creep coefficients.

TABLE 6: Mix proportion of concrete (kg/m³).

Cement	Water	Slag	Aggregate	Superplasticizer	Fly ash
460	180	85	1680	9.7	45

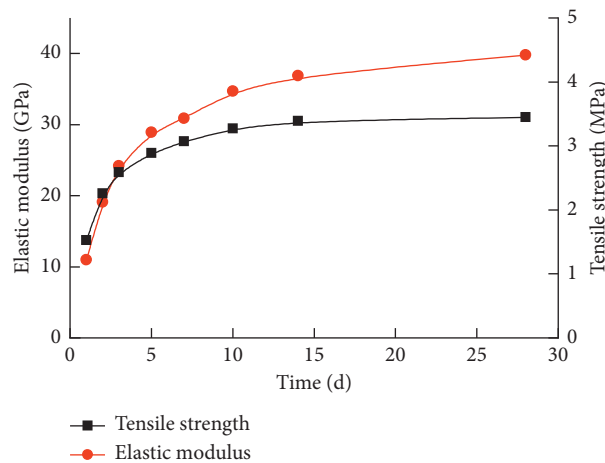


FIGURE 12: The mechanics parameters of box girder concrete.

and 0.2, respectively. The Lubliner criterion [31] is chosen to judge whether the concrete is cracked, as shown in (25).

6.3. Computational Results

6.3.1. Analysis of Temperature Field Calculation Results. Figure 15 shows a comparison between the measured data and the simulation results at measuring points 1 and 3. The simulated and measured results are consistent, indicating that the temperature field of the bridge is reflected in the simulation.

6.3.2. Analysis of Moisture Field Calculation Results. Figure 16 shows the humidity simulation results at points 1 and 3 under various calculation conditions. The results show that the humidity at the web center (point 3) is constant, mainly because the humidity conduction speed is too low, and the decrease in the humidity is mainly due to the cement hydration reaction. However, the humidity evolution on the web surface (point 1) is different, and the decrease in the humidity is mainly due to the humidity exchange with the environment. The lower the ambient humidity is, the higher the humidity gradient along the thickness of the web increases with time.

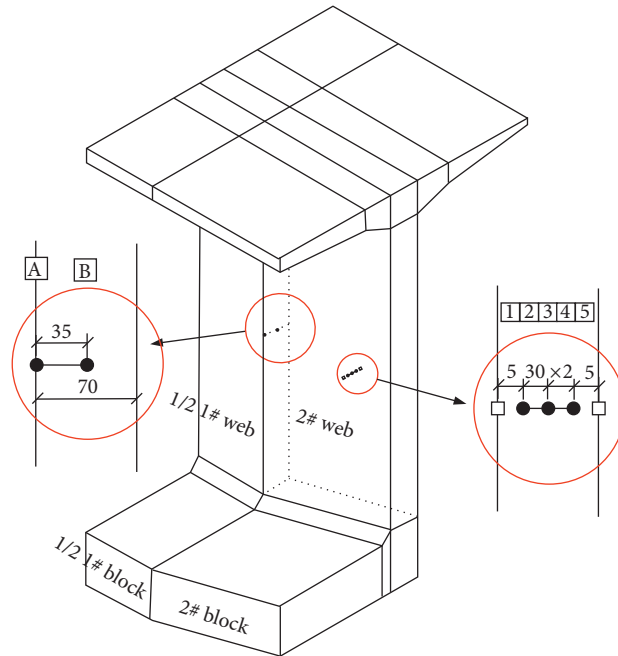


FIGURE 13: The hydration heat measured points and the positions of points A and B (unit: cm).

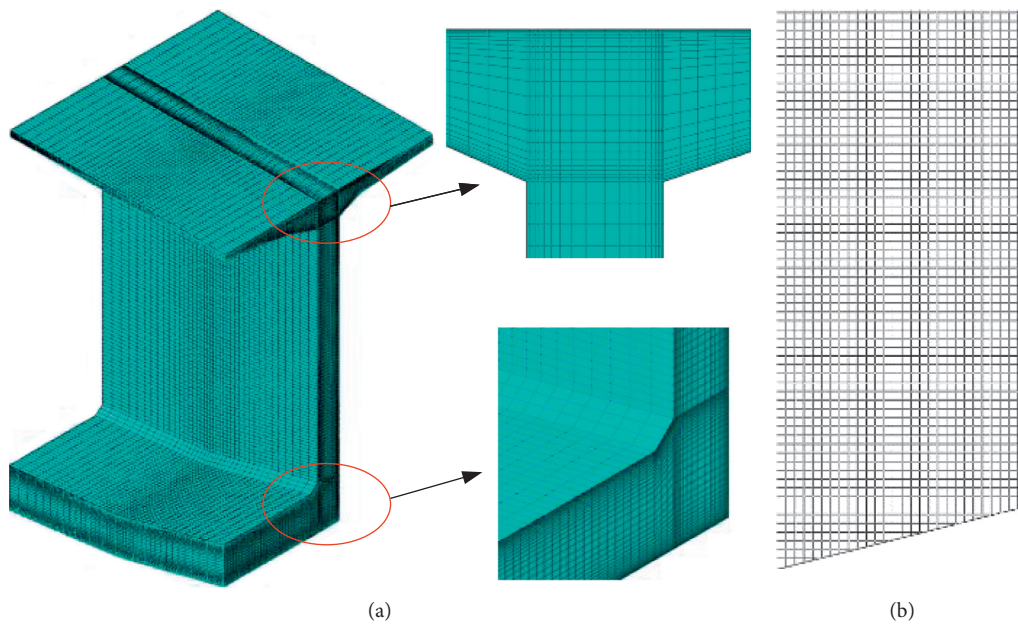


FIGURE 14: The finite element mesh model. (a) Concrete elements. (b) Rebar elements.

6.3.3. Analysis of Stress Field Calculation Results.

Figure 17 shows the web cracking simulation results under three calculation conditions; the web cracks are colored in red. The results show the following:

- (1) The cracks first appear at the interface, mainly because the free deformation of 2# block is restrained by 1# block.
- (2) The degree of web cracking under different humidity environments is different, indicating that the

external humidity environment has a significant impact on the mechanical behavior of the structure.

Based on whether the creep effect is considered or not, Figures 18 and 19 show the calculated values of the principal tensile stress at points 1 and 3 (in Figure 13). The results show that the creep can cause stress relaxation, which improves the crack resistance of the web. When considering the stress relaxation due to the creep and the crack resistance of the web reinforcement, the thermal moisture coupling effect

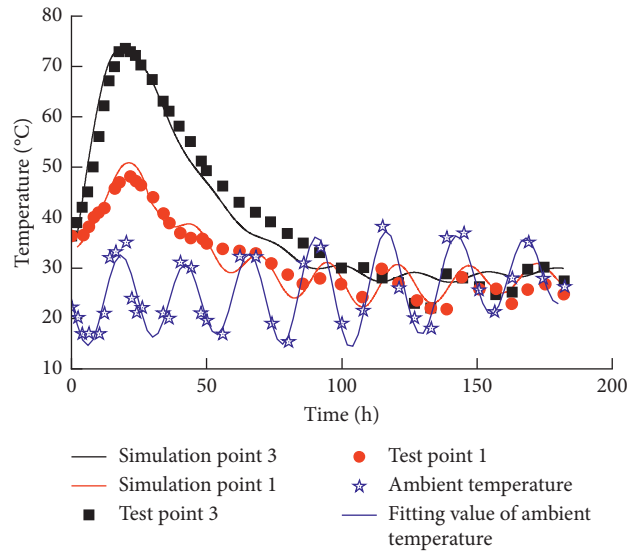


FIGURE 15: Comparison of simulated data and measured data on points 1 and 3.

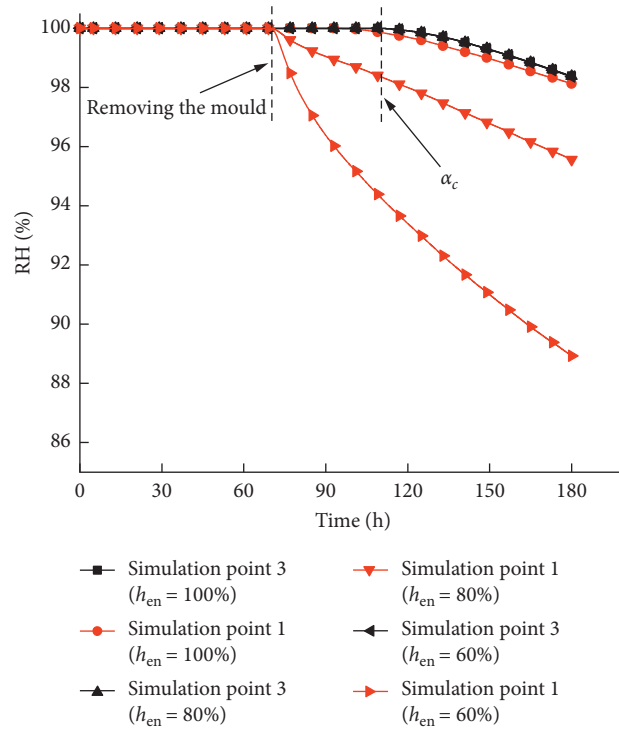


FIGURE 16: Comparison of simulated data on points 1 and 3.

does not cause any cracks at the center of the web (Figure 17).

Figure 20 shows the calculated values of the stress due to temperature and humidity at measuring points 1 and 3. For the temperature stress (in Figure 20),

- (1) The peak value is reached in approximately 33 h, because the temperature difference between the inside and outside of the web reaches the extreme value. However, the elastic modulus of the concrete is relatively low (approximately 14 GPa), and the

surface tensile stress due to the temperature gradient is approximately 0.9 MPa;

- (2) With the completion of hydration (at 95 h), the temperature field of the web is driven by the ambient temperature, and the temperature stress fluctuates with the change in the ambient temperature.

For humidity stress,

- (1) Before the removal of the mold, the cement hydration degree does not reach the critical hydration

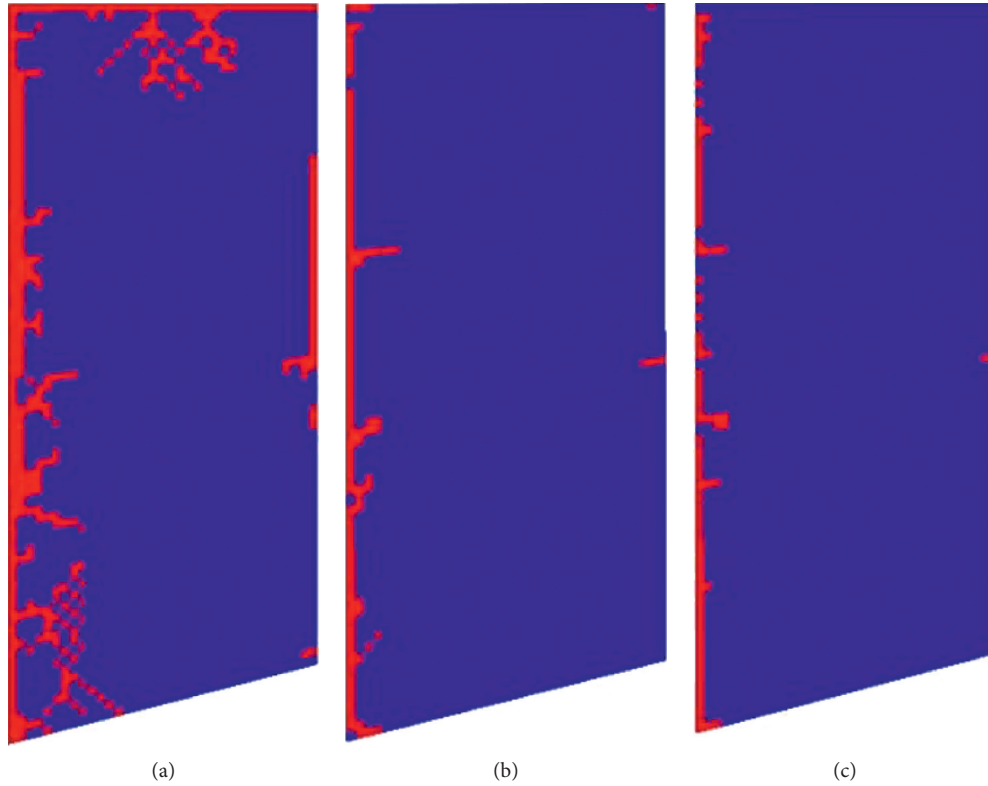


FIGURE 17: Comparison of the simulation results of web cracking under different working conditions. (a) $h_{en} = 60\%$. (b) $h_{en} = 80\%$. (c) $h_{en} = 100\%$.

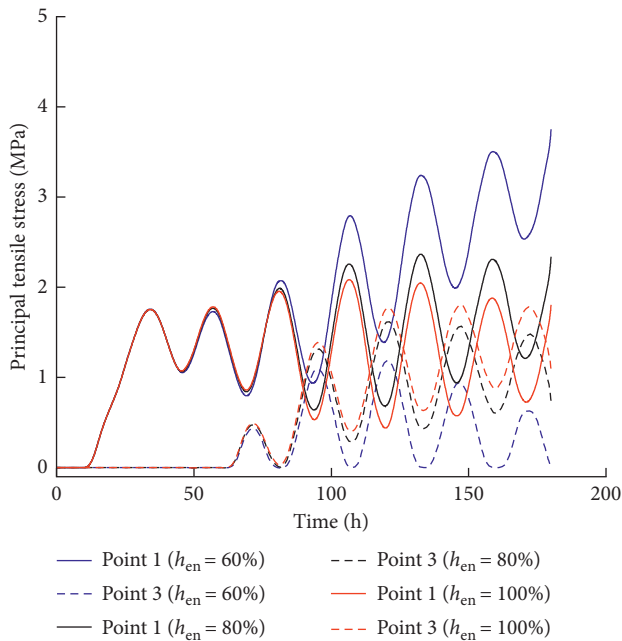


FIGURE 18: Comparison of time-dependent principal tensile stress distribution at points 1 and 3 (regardless of creep).

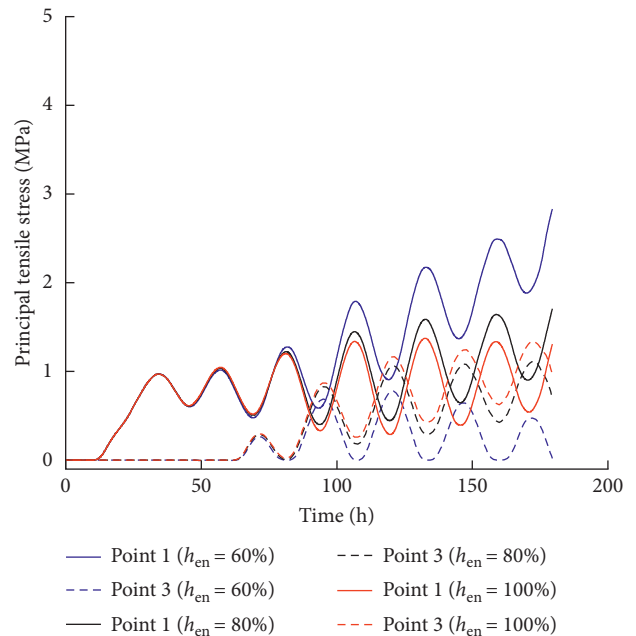


FIGURE 19: Comparison of time-dependent principal tensile stress distribution at points 1 and 3 (considering the creep).

degree α_c , and the internal humidity of the web remains in the first stage. In this stage, the humidity change law is not influenced by the external

environment humidity; therefore, the humidity stress under the different calculation conditions has the same evolution law;

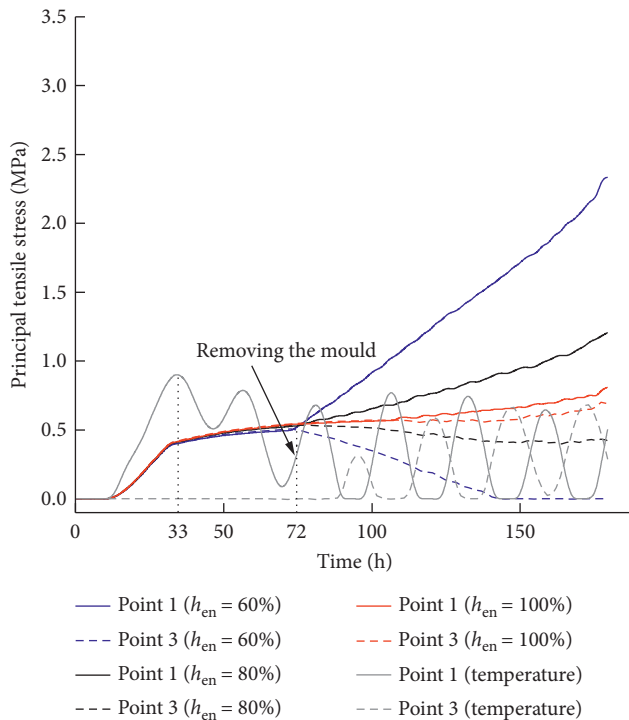


FIGURE 20: Comparison of time-dependent principal tensile stress caused by temperature and moisture.

- (2) After removing the mold (at 72 h), the surface layer of the web exchanges humidity with the environment, and the humidity gradient on the internal and external surfaces of the web increases with the age. When the environmental humidity is lower, the moisture conduction on the surface layer of the web is faster; however, the humidity at the center of the web is the same. Therefore, the humidity gradient along the thickness direction is higher, and the nonlinear distribution of the humidity gradient will make the web surface experience tension, and the center of the web is affected. With the decrease in the external humidity, the surface tensile stress increases, and the central tensile stress decreases. The calculation results, shown in Figure 19, confirm this rule;
- (3) When measures to preserve moisture are ineffective, the stress due to the humidity field will be significantly greater than that due to the temperature field.

7. Conclusion

A new method is proposed to analyze the thermo-hydro-mechanical combined effect during the construction of concrete beam bridges. A comparison between the calculation and test results shows that the proposed method can effectively simulate the combined effect of multifields under complex construction environments.

The humidity conduction rate is much lower than humidity conduction rate; even for thin-walled components, there remains a significant humidity gradient on the surface layer. When measures to avoid moisture are ineffective, the

stress due to the humidity field will be significantly greater than that due to the temperature field; therefore, more attention should be paid to the stages of design and construction maintenance.

For webs and other thin-walled components, the combined effect of humidity-induced shrinkage and the constraint on the early casted segment lead to cracks in the web.

With regard to the elastoplastic mechanics of concrete, the concrete in the crack area will produce not only creep deformation but also plastic deformation. It is necessary to establish a viscoplastic constitutive relationship that evolves with the concrete age; this requires further study.

Data Availability

The data used to support the findings of this study are available from the corresponding author upon request.

Conflicts of Interest

The authors declare no conflicts of interest.

Acknowledgments

This work was funded by China Postdoctoral Science Foundation (2020M672460) and the Major Scientific Research Projects of China Railway Siyuan Survey and Design Group Company Limited (2019K130).

References

- [1] S. W. Li, "Study on time-depending structural behavior of long-span cantilever casting PC box girder bridges based on thermo-hydro-mechanical combined effects analysis," Doctoral thesis, Southwest Jiaotong University, Chengdu, China, 2019.
- [2] S. W. Li, Q. Y. Yang, Q. H. Qian, D. Yang, B. L. Sun, and X. B. Li, "Three-dimensional nonlinear creep and shrinkage effects of a long-span prestressed concrete box girder bridge," *Structural Concrete*, vol. 20, no. 2, pp. 638–649, 2019.
- [3] A. Elsafty and A. Abdel-Mohti, "Investigation of likelihood of cracking in reinforced concrete bridge decks," *International Journal of Concrete Structures and Materials*, vol. 7, no. 1, pp. 79–93, 2013.
- [4] V. Gribniak, G. Kaklauskas, D. Čygas, D. Bačinskas, R. Kupliauskas, and A. Sokolov, "Investigation of concrete cracking effect in deck slab of continuous bridges," *The Baltic Journal of Road and Bridge Engineering*, vol. 5, no. 2, pp. 83–88, 2010.
- [5] K. V. L. Subramaniam, "Identification of early-age cracking in concrete bridge decks," *Journal of Performance of Constructed Facilities*, vol. 30, no. 6, pp. 1–9, 2016.
- [6] G. D. Li, "Mechanism and control for early-age shrinkage crack of HPC used for bridge engineering," Doctoral thesis, Harbin Institute of Technology, Harbin, China, 2014.
- [7] T. M. Wang, *Control of Cracking in Engineering Structure*, China Architecture & Building Press, Beijing, China, 2nd edition, 2017.
- [8] Y. Huang, G. Liu, S. Huang, R. Rao, and C. Hu, "Experimental and finite element investigations on the temperature field of a massive bridge pier caused by the hydration heat of concrete,"

- Construction and Building Materials*, vol. 192, pp. 240–252, 2018.
- [9] X. Hu, C. Shi, Z. Shi, B. Tong, and D. Wang, “Early age shrinkage and heat of hydration of cement-fly ash-slag ternary blends,” *Construction and Building Materials*, vol. 153, pp. 857–865, 2017.
- [10] S. E. Giuseppe, “Thermo-hygro-chemo-mechanical model of concrete at early ages and its extension to tumor growth numerical analysis,” Doctoral thesis, Università Degli Studi Di Padova, Cachan, France, 2013.
- [11] F.-J. Ulm and O. Coussy, “Modeling of thermo-chemo-mechanical couplings of concrete at early ages,” *Journal of Engineering Mechanics*, vol. 121, no. 7, pp. 785–794, 1995.
- [12] F.-J. Ulm and O. Coussy, “Strength growth as chemo-plastic hardening in early age concrete,” *Journal of Engineering Mechanics*, vol. 122, no. 12, pp. 1123–1132, 1996.
- [13] M. Cervera, J. Oliver, and T. Prato, “Thermo-chemo-mechanical model for concrete. I: hydration and aging,” *Journal of Engineering Mechanics*, vol. 125, no. 9, pp. 1018–1027, 1999.
- [14] M. Cervera, J. Oliver, and T. Prato, “Thermo-chemo-mechanical model for concrete. II: damage and creep,” *Journal of Engineering Mechanics*, vol. 125, no. 9, pp. 1028–1039, 1999.
- [15] R. Lackner and H. A. Mang, “Chemoplastic material model for the simulation of early-age cracking: from the constitutive law to numerical analyses of massive concrete structures,” *Cement and Concrete Composites*, vol. 26, no. 5, pp. 551–562, 2004.
- [16] D. Gawin, B. A. F. Pesavento, and B. A. Schrefler, “Hygro-thermo-chemo-mechanical modelling of concrete at early ages and beyond. Part I: hydration and hygro-thermal phenomena,” *International Journal for Numerical Methods in Engineering*, vol. 67, no. 3, pp. 299–331, 2006.
- [17] D. Gawin, B. A. F. Pesavento, and B. A. Schrefler, “Hygro-thermo-chemo-mechanical modelling of concrete at early ages and beyond. Part II: shrinkage and creep of concrete,” *International Journal for Numerical Methods in Engineering*, vol. 67, no. 3, pp. 332–363, 2006.
- [18] G. Di Luzio and G. Cusatis, “Solidification-microprestress-microplane (SMM) theory for concrete at early age: theory, validation and application,” *International Journal of Solids and Structures*, vol. 50, no. 6, pp. 957–975, 2013.
- [19] W. Cui, W. Chen, and N. Wang, “Thermo-hydro-mechanical coupling analysis of early-age concrete with behavioral changes considered and its application,” *China Civil Engineering Journal*, vol. 48, no. 2, pp. 44–53, 2015.
- [20] Z. Ge, *Predicting Temperature and Strength Development of the Field Concrete*, Doctoral thesis, Iowa State University, Ames, IA, USA, 2005.
- [21] B. F. Zhu, *Thermal Stresses and Temperature Control of Mass Concrete*, pp. 13–30, Tsinghua University Press, Beijing, China, 2012.
- [22] Y. Lee, M.-S. Choi, S.-T. Yi, and J.-K. Kim, “Experimental study on the convective heat transfer coefficient of early-age concrete,” *Cement and Concrete Composites*, vol. 31, no. 1, pp. 60–71, 2009.
- [23] J. Zhang, K. Qi, and Y. Huang, “Calculation of moisture distribution in early-age concrete,” *Journal of Engineering Mechanics*, vol. 135, no. 8, pp. 871–880, 2009.
- [24] CEB-FIP, *CEB-FIP Model Code 2010*, International Federation for Structural Concrete (fib), Lausanne, Switzerland, 2012.
- [25] M. A. Oliveira, M. Azenha, and P. B. Lourenço, “Simulation of humidity fields in concrete: experimental validation and parameter estimation,” *Journal of Advanced Concrete Technology*, vol. 13, no. 4, pp. 214–229, 2015.
- [26] T. Kanstad, T. A. Hammer, Ø. Bjøntegaard, and E. J. Sellevold, “Mechanical properties of young concrete: Part II: determination of model parameters and test program proposals,” *Materials and Structures*, vol. 36, no. 4, pp. 226–230, 2003.
- [27] J. Zhang, H. Dongwei, and S. Wei, “Experimental study on the relationship between shrinkage and interior humidity of concrete at early age,” *Magazine of Concrete Research*, vol. 62, no. 3, pp. 191–219, 2010.
- [28] Z. P. Bazant and L. Panula, “Practical prediction of time dependent deformation of concrete, Parts I and II,” *Mater. Struct.* vol. 11, no. 65, pp. 307–328, 1978.
- [29] G. M. Ji, “Cracking risk of concrete structures in the hardening phase: experiments, material modeling and finite element analysis,” Doctoral thesis, The Norwegian University of Science and Technology, Trondheim, Norway, 2008.
- [30] M. Azenha, L. Leitão, J. L. Granja, C. de Sousa, R. Faria, and J. A. O. Barros, “Experimental validation of a framework for hydro-mechanical simulation of self-induced stresses in concrete,” *Cement and Concrete Composites*, vol. 80, pp. 41–54, 2017.
- [31] J. Lubliner, J. Oliver, S. Oller, and E. Oñate, “A plastic-damage model for concrete,” *International Journal of Solids and Structures*, vol. 25, no. 3, pp. 299–326, 1989.
- [32] G. Yao, Z. J. Yu, Y. Yang, and W. Jia, “Study on temperature field and temperature stress of single-cell box girder cured with electric heater,” *China Civil Engineering Journal*, vol. 51, no. 3, pp. 109–114, 2018.
- [33] J. Zhang, D. W. Hou, and Y. Gao, “Uniform driving force for autogenous and drying shrinkage of concrete,” *Journal of Tsinghua University (Science and Technology)*, vol. 50, no. 9, pp. 1321–1324, 2010.
- [34] I. Khan, A. Castel, and R. I. Gilbert, “Tensile creep and early-age concrete cracking due to restrained shrinkage,” *Construction and Building Materials*, vol. 149, pp. 705–715, 2017.
- [35] J. Q. Wang and Z. Fang, “Study on early crack in the web of long-span PC box girder bridge,” *Journal of Hunan University Natural Sciences*, vol. 39, no. 5, pp. 6–12, 2012.